Malaysian Journal of Chemistry, 2025, Vol. 27(6), 96-107

Novel Salicylaldehyde-Bound Schiff Base-Capped Zinc Sulphide Nanoparticles as a Highly Selective and Sensitive Fluorescent Sensor for Ferric Ions

Meera Jacob[1,2]* and Jaya T. Varkey[2]
[1]Department of Chemistry, St. Paul's College, Ernakulam - 683 503, Kochi, Kerala, India
[2]Department of Chemistry, St. Teresa's College, Ernakulam - 682 035, Kochi, Kerala, India
*Corresponding author (e-mail: meera@stpauls.ac.in)

Highly fluorescent salicylaldehyde-bound Schiff base-capped zinc sulphide nanoparticles were synthesised by treating the Schiff base, N-Hexadecylsalicylideneamine (L^1), with a solution containing zinc salt and a reducing agent. The synthesised Schiff base-capped zinc sulphide nanoparticles (L^1@ZnS NPs) were characterised by ultraviolet-visible (UV-Vis) absorption spectroscopy, photoluminescence (PL) spectroscopy, and transmission electron microscopy (TEM). The L^1@ZnS NPs were found to be a selective and sensitive fluorescent probe for the determination of ferric [Fe (III)] ions. The fluorescent sensor displayed a linear response in the range from 0.149 μM to 1.47 μM, with the limit of detection (LOD) and limit of quantification (LOQ) of 0.093 μM and 0.282 μM, respectively.

Keywords: Schiff base; fluorescent; nanoparticles; zinc sulphide; ferric ion

Received: July 2025; Accepted: August 2025

The most prevalent transition metal ion in cellular systems is iron(III), which is vital for many biological functions, including oxygen transport in haemoglobin [1], cellular metabolism [2], catalysis, and serving as a co-factor in enzyme-mediated reactions [3–8]. An imbalance of iron, either deficiency or excess, can impair cellular function and lead to various diseases, such as Parkinson's disease [9], Huntington's disease [10–11], renal impairment [12–15], Alzheimer's disease [16–18], anaemia [19–20], cancer [10, 21–22], diabetes [10, 23], liver disorders [24-25], heart failure, and arthritis [6,10]. Consequently, the detection and quantification of Fe(III) are crucial for the early identification of these diseases.

Various methods have been used for the determination of iron, like voltammetry [26], potentiometry [27], flame atomic absorption spectrometry (FAAS), atomic absorption spectrometry [28], inductively coupled plasma mass spectroscopy (ICPMS) [29], and inductively coupled plasma atomic emission spectrometry (ICP-AES) [28, 30]. Among these analytical approaches, fluorescence signal analysis has emerged as an effective method because of its advantages, which include ease of use [31], high sensitivity [32], real-time monitoring, affordability, and rapid detection and quantification of metal ions [30].

At the forefront of materials science research, nanoparticles are becoming more and more ingrained in our daily lives [33]. Increased surface to volume ratio [34], enhanced activity, superior anti-photobleaching qualities, and tuneable emission characteristics of nanomaterials have attracted significant interest for use in chemical sensors [35]. Band gap energy is essential for comprehending the electrical and optical properties of materials. At nanoscale, any change in the band gap of a nanoparticle has a direct impact on the properties of the material [36]. Hence, band gap energy must be considered in nanomaterial science and technology [37]. With a broad band gap of roughly 3.72 eV to 3.78 eV, zinc sulphide nanoparticles (ZnS NPs), a prospective low-toxicity semiconductor material, exhibit exceptional optical and electrical capabilities [38–41]. Due to these characteristics, ZnS NPs represent a promising candidate for the development of novel sensors.

Capping agents are vital stabilisers that hinder the aggregation of nanoparticles during their colloidal synthesis. These surface functionalising agents determine the properties of the nanoparticles [42]. The role of Schiff base as a stabilising agent, particularly for ZnS NPs, remains underexplored and scarcely reported. The incorporation of Schiff base can facilitate the regulation of morphology, structure, and luminescent and optical properties [43].

Here, we report a novel fluorescent probe, L^1@ZnS NPs, for the determination of Fe(III) ions. The developed sensor was observed to be stable for approximately 30 minutes. Upon adding Fe(III) ions, a noticeable quenching of the fluorescence of the fluorophore was shown, and the probe exhibited a remarkable linear range.

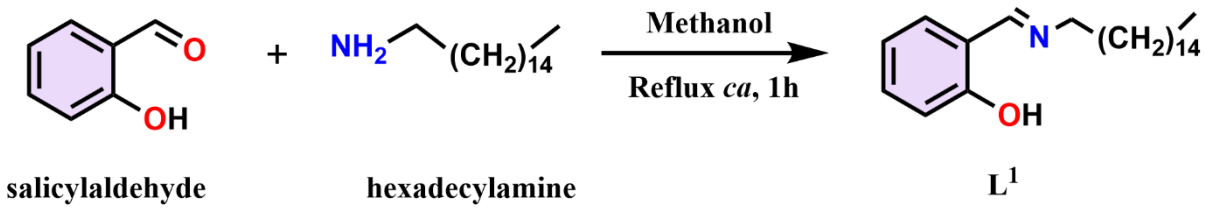

Scheme 1. Synthesis of L^1.

EXPERIMENTAL

Chemicals and Materials

Methanol, hexadecylamine, salicylaldehyde, zinc acetate dihydrate, sodium sulphide nonahydrate, manganese(II) chloride tetrahydrate, nickel(II) chloride hexahydrate, aluminium chloride, copper(II) chloride hexahydrate, lead acetate monohydrate, magnesium chloride hexahydrate, ferric chloride hexahydrate, cobalt(II) chloride hexahydrate, mercuric acetate, and ferrous chloride tetrahydrate purchased were of analytical grade and used without further purification.

Characterisation Method

The Proton Nuclear Magnetic Resonance (^{1}H NMR) spectrum of L^1 was obtained on a Bruker Avance III HD 500 spectrometer. The high-resolution mass spectrum (HRMS) of L^1 was obtained using a Thermo scientific Q exactive mass spectrometer employing electron spray ionisation (ESI) technique. The electronic and PL spectra were recorded on Shimadzu UV-3600 UV-VIS-NIR and Horiba Fluorolog3 FL-1057 model spectrometers, respectively. TEM images were recorded using a JEM- 2100 HRTEM.

Synthesis of L^1

The synthesis of L^1 has been reported previously in the literature [44]. 5 mmol of hexadecylamine dissolved in 5 mL of methanol was added dropwise to 5 mL of methanolic solution containing 5 mmol of salicylaldehyde. The resulting yellow coloured solution was refluxed at 100°C under constant stirring for 1 hour (Scheme 1). The solution was then allowed to cool to room temperature and subsequently poured into ice. The resulting yellow precipitate was filtered and recrystallised using ethanol. The recrystallised product was then dried over anhydrous calcium chloride.

Synthesis of L^1@ZnS NPs

The L^1@ZnS NPs were synthesised following a synthetic route published earlier with minor modifications [45]. 25 mL of 0.25 M $Na_2S.9H_20$ and 25 mL of 0.25 M zinc acetate were dissolved in Milli-Q water in separate beakers. These solutions were stirred for 30 minutes. 0.01 mmol of the L^1 was dissolved in 10 mL of methanol and added to the zinc salt solution. The sodium sulphide solution was added dropwise to the reaction mixture after 30 minutes. The beaker was kept aside for another 30 minutes. The synthesised L^1@ZnS NPs were subjected to multiple rounds of centrifugation at 10,000 revolutions per minute for purification, after which the resulting particles were redispersed in Millipore water.

Preparation of Fe(III) Solution

A stock solution of ferric chloride with a concentration of 1 mM was prepared in Milli-Q water. This stock solution was then further diluted to obtain Fe(III) solutions of different concentrations.

Analytical Procedure

2 mL of the prepared L^1@ZnS NPs solution was taken and a suitable amount of Fe(III) solution was added. The intensity of fluorescence emission was then measured. I_0 and I denote the emission intensity of the probe before and after the addition of Fe(III), respectively. All measurements were carried out at ~pH 6.7 and ambient temperature.

RESULTS AND DISCUSSION

Characterisation of L^1

The synthesised L^1 was characterised by mass spectrometry and ^{1}H NMR spectroscopy. The examination of the ESI-HRMS spectrum of L^1, as shown in **Figure 1**, reveals that the observed mass-to-charge ratio (m/z) value of $[M+H]^+$ for $C_{23}H_{39}NO$ (346.3120) is in strong agreement with the calculated value (346.3110). The ^{1}H NMR spectrum of L^1 was recorded with $CDCl_3$ as solvent and is depicted in **Figure 2**. The singlet peak at δ 8.32 ppm corresponds to the azomethine (–CH=N–) proton. The aromatic protons resonate in the region of 7.33-6.85 ppm and appear as a multiplet. A triplet in the upfield region around 0.89-0.86 ppm indicates the terminal methyl group. The methylene protons adjacent to azomethine nitrogen (–CH_2–N=C–) give rise to a triplet in the region 3.62-3.59 ppm [46]. The remaining methylene protons appear as multiplets in the region of 1.70-1.25 ppm. The spectral investigations confirmed the formation of L^1.

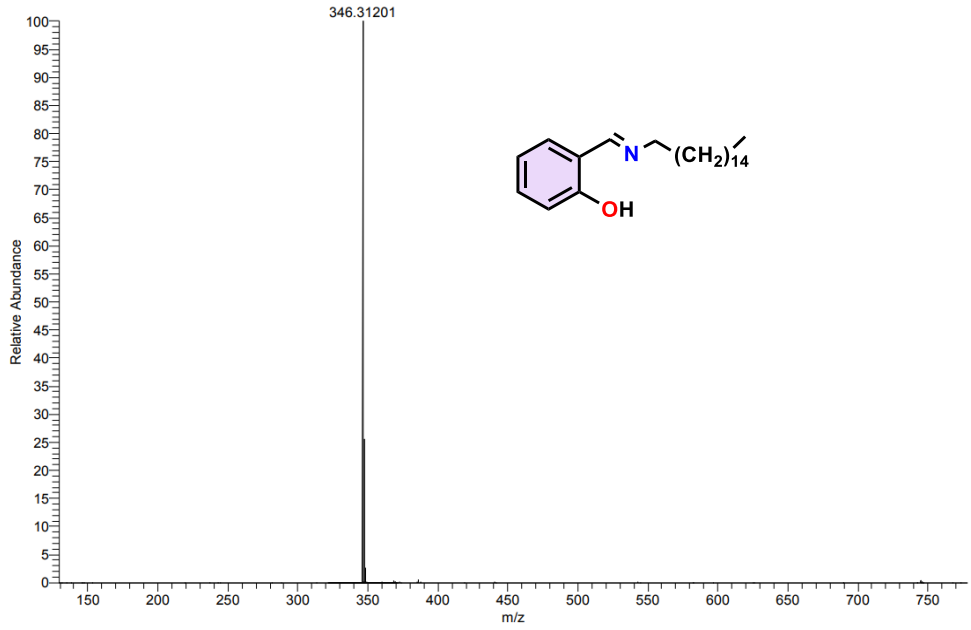

Figure 1. HR-MS spectrum of L^1.

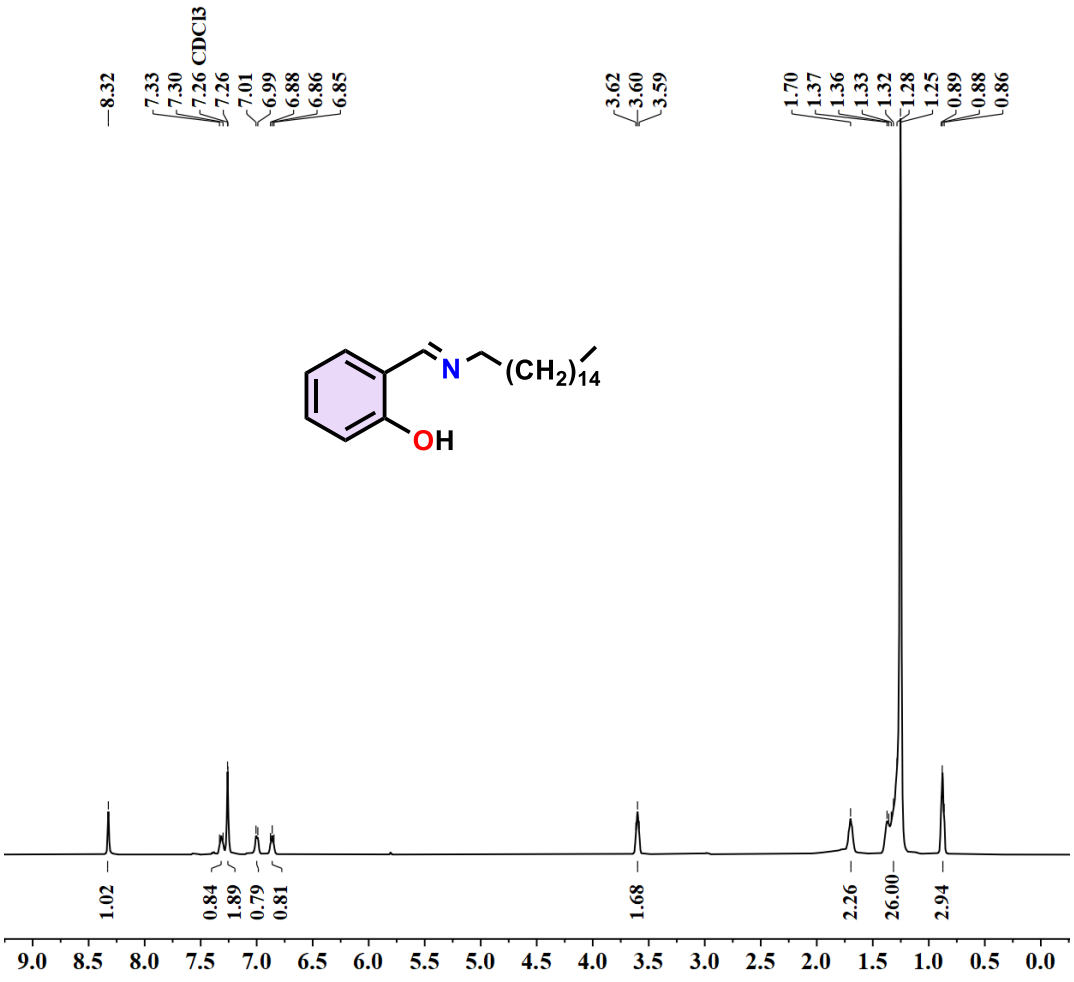

Figure 2. ^{1}H NMR spectrum of L^1.

Characterisation of L^1@ZnS NPs

Characterisation of the synthesised L^1@ZnS NPs was carried out through UV-Vis absorption spectroscopy, fluorescence spectroscopy, and TEM. The absorption spectrum of the L^1@ZnS NPs exhibits an absorption maximum centred around 340 nm (**Figure 3**). The emission spectrum of the L^1@ZnS NPs was centred at 419 nm (**Figure 4**). The surface morphology of the prepared L^1@ZnS NPs was analysed using TEM. The TEM image (**Figure 5(a)**) reveals that the ZnS NPs are nearly spherical shape, with an average size of approximately 30 nm. The lattice fringes are visible in the high-resolution TEM (HRTEM) image (**Figure 5(b)**) and the selected area electron diffraction (SAED) pattern (inset in **Figure 5(b)**) suggests the polycrystalline structure of the prepared nanoparticles.

Fluorescence Quenching of L^1@ZnS NPs by Fe(III)

The L^1@ZnS NPs showed a fluorescence emission at 416 nm when excited at 350 nm. A significant decrease in the emission intensity was observed upon the addition of Fe(III) (**Figure 6**). As the concentration of Fe(III) increased, the fluorescence intensity of the probe continued to decline.

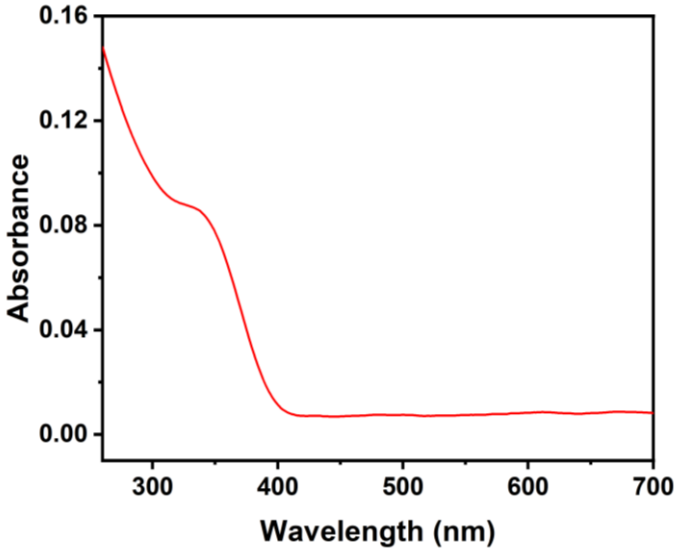

Figure 3. Absorption spectrum of L^1@ZnS NPs.

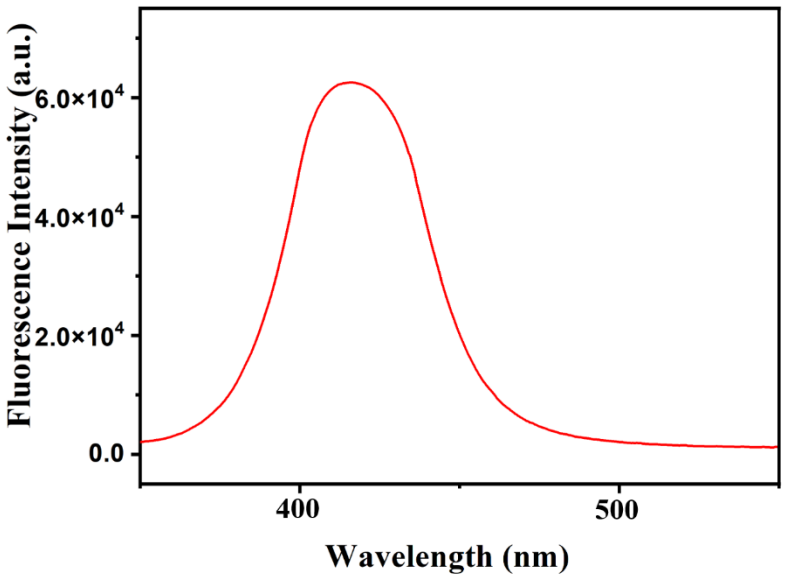

Figure 4. Fluorescence emission spectrum of L^1@ZnS NPs.

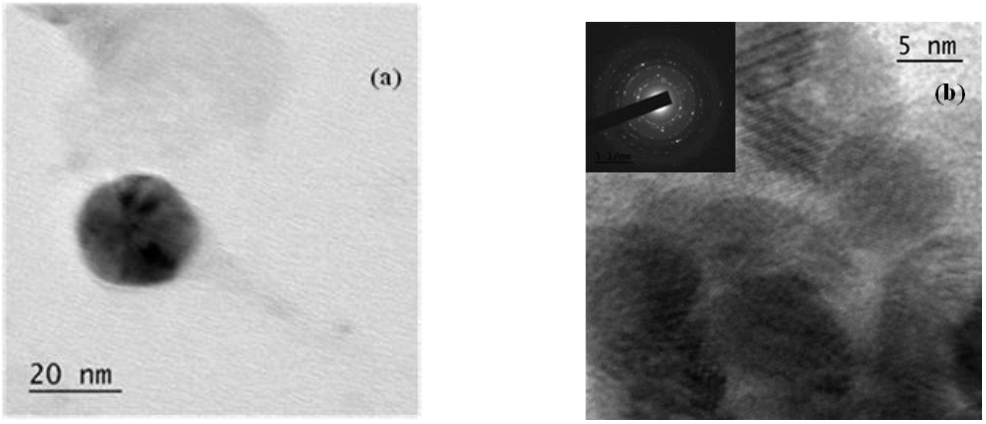

Figure 5. (a) TEM and **(b)** HRTEM (inset: SAED) images of L^1@ZnS NPs.

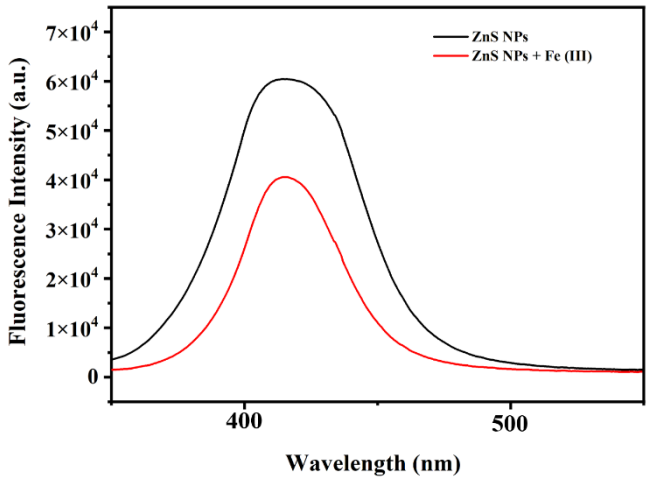

Figure 6. Fluorescence spectra of L^1@ZnS NPs before and after the addition of 1.18 μM Fe(III).

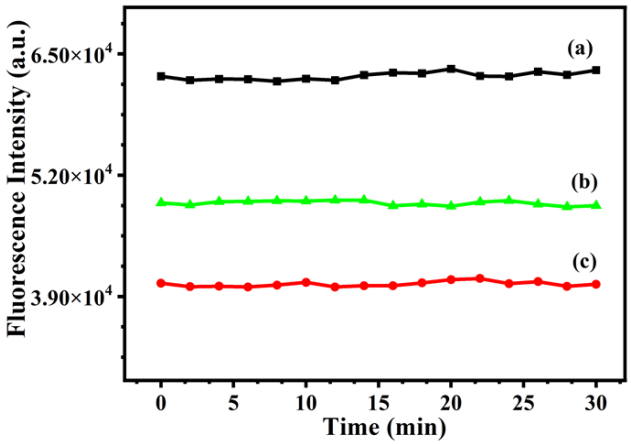

Figure 7. Influence of time on the emission intensity of (a) L^1@ZnS NPs, (b) L^1@ZnS NPs + 0.596 μM Fe(III), and (c) L^1@ZnS NPs + 1.18 μM Fe(III).

Effect of Time

By measuring the intensity of the proposed assay at regular intervals before and after the addition of different concentrations of Fe(III), the impact of time on the intensity of emission of L^1@ZnS NPs – Fe(III) was examined (**Figure 7**). It is clear from the results that the reaction between L^1@ZnS NPs and Fe(III) took place instantly and the intensity of photoluminescence dropped to a minimum immediately. The intensity of the fluorophore remains almost constant for about 30 minutes.

Sensitivity Study

The emission intensity of the L^1@ZnS NPs decreased steadily with increasing concentrations of Fe(III) (**Figure 8**). The relationship between the intensity of L^1@ZnS NPs and the concentration of Fe(III) is explained by the Stern-Volmer equation and the calibration curve, i.e., the plot of the relative intensity of fluorescence (I_0/I) as a function of concentration of Fe(III), was found to be linear within the range from 0.149 µM to 1.47 µM (**Figure 9**). The LOD and LOQ calculated were found to be of 0.093 µM and 0.282 µM, respectively. The dependence of concentration (C) on the relative intensity of emission (I_0/I) follows the equation:

$$I_0 / I = 0.488141C + 0.9634 \text{ , } R^2 = 0.9964$$

The relative standard deviation (RSD) of 1.5% from six repeated measurements (L^1@ZnS NPs + 1.47 µM of Fe(III)) indicates the high reproducibility of the developed method. The performance of the proposed fluorescent sensor was evaluated in comparison to previously reported Fe(III) sensors (**Table 1**). The analysis of the results reveals that the developed sensor demonstrates performance superior to that of existing sensors in regard to linear range and LOD.

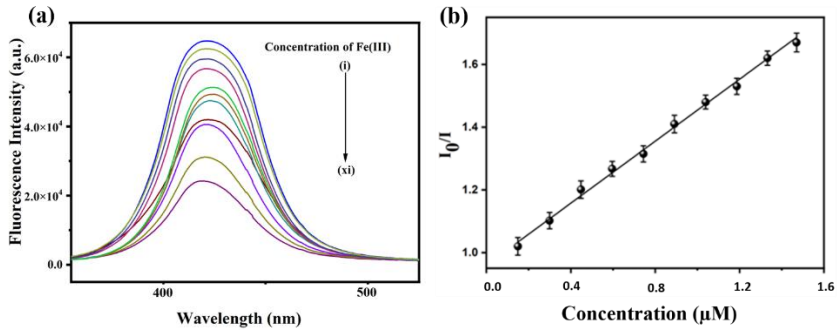

Figure 8.
(a) Fluorescence spectra of L^1@ZnS NPs in the presence of Fe(III) at concentrations of (i) 0 µM, (ii) 0.149 µM, (iii) 0.299 µM, (iv) 0.447 µM, (v) 0.596 µM, (vi) 0.744 µM, (vii) 0.891 µM, (viii) 1.03 µM, (ix) 1.18 µM, (x) 1.33 µM, and (xi) 1.47 µM.
(b) Stern-Volmer plot for the quenching process from 0.149 µM to 1.47 µM concentrations of Fe(III).

Table 1. Comparative analysis of fluorescent sensors for Fe(III).

Fluorescent sensor	Linear range (µM)	LOD (µM)	Reference
Carbon dot derived from coffee waste	0–100	4.31	[47]
S-doped silicon quantum dots	1–20	0.210	[48]
Schiff base-ZnS NPs	10–500	10.2	[49]
*PFM	0–3	0.12	[50]
Dopamine Functionalized S, N Co-doped Carbon Dots	5– 200	2.86	[51]
Proposed sensor	0.149 –1.47	0.093	This work

*5-(4-methoxyphenyl) -3-(5-methylfuran-2-yl) -1- phenyl-4,5-dihydro-1H-pyrazole

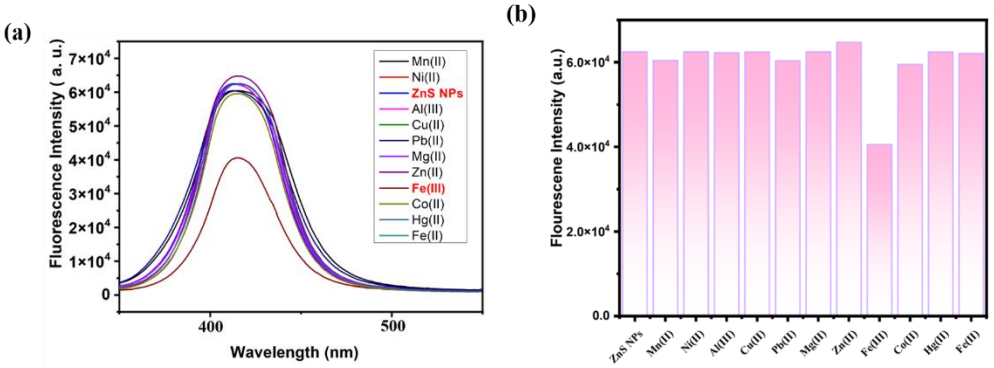

Figure 9 (a) & (b). Selective suppression of the fluorescence in L^1@ZnS NPs by Fe(III**)**.

Selectivity

The key feature of any chemical sensor is to selectively detect the analyte [52]. The emission behaviour of our probe was studied in the presence of various biologically significant metal ions, each at a concentration of 1.18 μM. The tested ions included Mn(II), Ni(II), Al(III), Cu(II), Pb(II), Mg(II), Zn(II), Co(II), Hg(II), and Fe(II). While most of these ions are either essential or toxic elements typically found in biological environments, Al(III) was also considered despite its lack of biological necessity, owing to its trivalent charge and potential to interfere with Fe(III) detection. Among these, only Fe(III) was able to profoundly diminish the emission intensity of the probe, demonstrating remarkable selectivity for the Fe(III) ion over other cations. In **Figure 9(a)**, the photoluminescence of ZnS NPs serves as the control, providing a baseline for comparison with the responses observed upon the addition of various cations. A quantitative representation of this data is shown as a bar graph in **Figure 9(b)**.

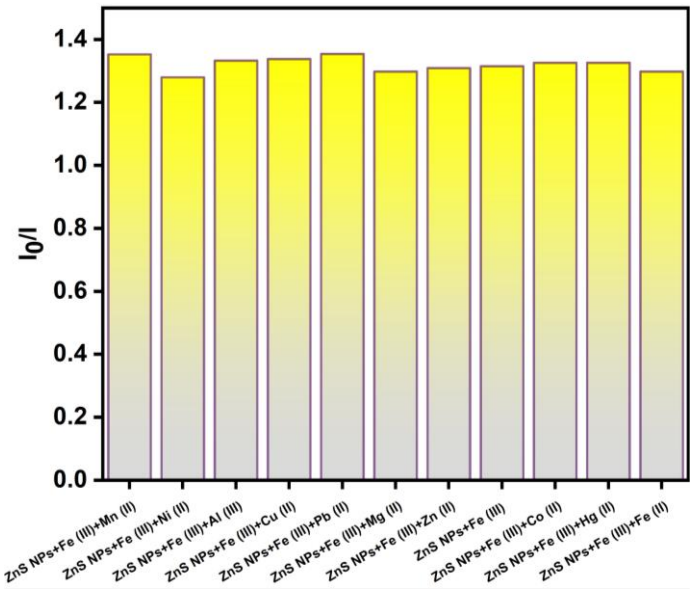

Figure 10. Bar diagram depicting the fluorescence signal of L^1@ZnS NPs in the presence of other cations at a 10-fold excess of concentration.

Table 2. Effect of foreign species on the luminescence signal of the probe in the presence of Fe(III) (0.744 µM).

Foreign Species	Concentration (µM)	Signal change %
Ni(II)	74.4	1.5
Pb(II)	74.4	0.8
Zn(II)	74.4	0.3
Al(III)	74.4	3.2
Co(II)	74.4	2.3
Mg(II)	74.4	3.7
Mn(II)	74.4	3.3
Fe(II)	74.4	4.5
Cu(II)	74.4	4.1
Hg(II)	22.3	2.9

Interference Study

A study was conducted to examine the impact of the concentration of the above-mentioned cations on the fluorescence intensity of L^1@ZnS NPs containing 0.744 µM Fe(III) ion. Fluorescence signals of the probe in the presence of Fe(III) were measured at different concentrations of the other cations: one-fold (0.744 µM), ten-fold (7.44 µM) and hundred-fold (74.4 µM) excess of the concentration of Fe(III) ions. **Figure 10** shows the effect of the cations at 10-fold excess of the concentration of Fe(III) on the intensity of emission of the probe. The results reveal that none of the cations, except for Hg(II), caused any significant interference, even at a 100-fold excess concentration compared to Fe(III). Hg(II) at concentrations above a 30-fold excess relative to Fe(III) demonstrated a signal variation exceeding 5% (**Table 2**).

Mechanism of Quenching

It is clear from **Figure 6** that the luminescence intensity of the probe is reduced by the addition of Fe(III) ions. The possible mechanism for the quenching of fluorescence was investigated. The quenching mechanisms include static, dynamic or a combination of both [53].

The plot between relative intensity against concentration of the quencher, known as the Stern-Volmer plot, would be linear if the process operates through a static or dynamic mechanism, and would be non-linear if it involves a combination of both [53, 54–55]. From the linear calibration curve in our study (**Figure 9**), it is evident that a combined static and dynamic quenching mechanism can be ruled out.

Moreover, the quenching constant for dynamic quenching process is typically less than 100 $Lmol^{-1}$, whereas for static quenching, it typically exceeds 100 $Lmol^{-1}$ [53]. The quenching constant obtained (**Figure 9**) is found to be 4.88141×10^5 $Lmol^{-1}$, indicating that the mechanism is more likely to be static quenching.

To gain further insights into the mechanism, we recorded the UV-Vis spectra of the L^1@ZnS NPs in the absence and presence of Fe(III). A noticeable change in the absorption band of the fluorophore in the presence of the quencher is indicative of complex formation and is a distinctive feature of static quenching [56–57]. It is evident from **Figure 11** that there is a red shift in the absorption wavelength of the L^1@ZnS NPs after the addition of Fe(III), providing additional evidence for static quenching.

Here, the fluorophore interacts with the quencher to form a non-emissive ground-state charge-transfer complex [58]. The partially filled d-orbitals of Fe(III) can accept electrons from the oxygen-containing functional groups on the L^1@ZnS NPs due to hard acid-hard base interaction, resulting in the drop of luminescence intensity of the probe [47, 59].

The interference of Hg(II) in Fe(III) detection, observed at concentrations exceeding a 30-fold excess, is presumably due to its strong binding affinity toward the electron-rich surface of the L^1@ZnS NPs [60].

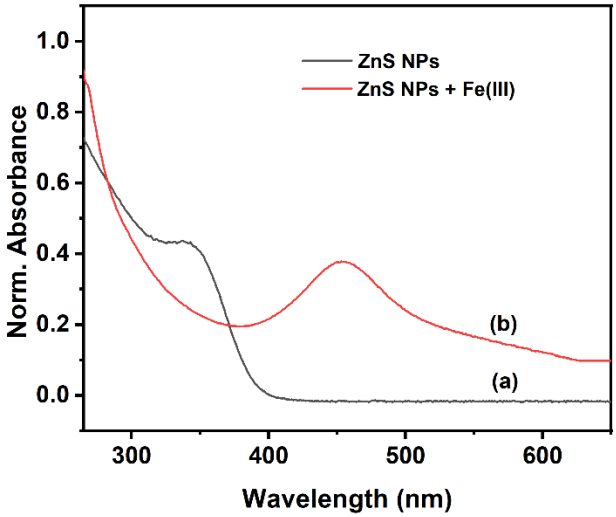

Figure 11. Absorption spectra of (a) L^1@ZnS NPs and (b) L^1@ZnS NPs + Fe(III) ions.

CONCLUSION

A Schiff base ligand was prepared by the condensation reaction of salicylaldehyde and hexadecylamine and was characterised using mass spectrometry and ^1H NMR spectroscopy. ZnS NPs stabilised with this ligand were synthesised and characterised using UV-Vis spectroscopy, PL, and TEM. The synthesised Schiff base-stabilised ZnS NPs could act as a fluorescent probe for the determination of Fe(III) ions. The proposed assay exhibited a linear range from 0.149 µM to 1.47 µM with LOD and LOQ of 0.093 µM and 0.282 µM, respectively. The developed sensor displayed high selectivity and sensitivity for Fe(III) ions, with static quenching identified as the mechanism.

ACKNOWLEDGEMENT

The authors gratefully express their profound gratitude to the Department of Chemistry, St. Paul's College, Kalamassery and the Department of Chemistry, St. Teresa's College, Ernakulam for their steadfast support and cooperation. The facilities and guidance provided by both departments were instrumental in the successful completion of this work.

REFERENCES

1. Ciaccio, C., Coletta, A. and Coletta, M. (2022) Role of hemoglobin structural-functional relationships in oxygen transport. *Molecular Aspects of Medicine*, **84**, 101022.

2. Wang, J. and Pantopoulos, K. (2011) Regulation of cellular iron metabolism. *Biochemical Journal*, **434(3)**, 365–381.

3. Eisenstein, R. S. (2000) Iron regulatory proteins and the molecular control of mammalian iron metabolism. *Annual Review of Nutrition*, **20**, 627–662.

4. Rouault, T. A. (2006) The role of iron regulatory proteins in mammalian iron homeostasis and disease. *Natural Chemical Biology*, **2(8)**, 406–414.

5. Hentze, M. W., Muckenthaler, M. U., Galy, B. and Camaschella, C. (2010) Two to tango: regulation of Mammalian iron metabolism. *Cell*, **142(1)**, 24–38.

6. Song, P., Zhang, L., Long, H., Meng, M., Liu, T., Yin, Y. and Xi, R. (2017) A multianalyte fluorescent carbon dots sensing system constructed based on specific recognition of Fe(III) ions. *RSC Advances*, **7(46)**, 28637–28646.

7. Walczyk. T. and von Blanckenburg, F. (2002) Natural Iron Isotope Variations in Human Blood. *Science*, **295 (5562)**, 2065–2066.

8. D'Autréaux, B., Tucker, N. P., Dixon, R. and Spiro, S. (2005) A non-haem iron centre in the transcription factor NorR senses nitric oxide. *Nature*, **437 (7059)**, 769–772.

9. Jiang, H., Wang, J., Rogers, J. and Xie, J. (2017) Brain Iron Metabolism Dysfunction in Parkinson's Disease. *Molecular Neurobiology*, **54(4)**, 3078.

10. Ru, Q., Li, Y., Chen, L. Wu, Y., Min, J. and Wang, F. (2024) Iron homeostasis and ferroptosis in human diseases: mechanisms and therapeutic prospects. *Signal Transduction and Targeted Therapy*, **9(1)**, 1–64.

11. Niu, L., Zhou, Y., Wang, J. and Zeng, W. (2024) Nuclear translocation of STAT5 initiates iron overload in huntington's disease by up-regulating IRP1 expression. *Metabolic Brain Disease*, **39(4)**, 559–567.

12. Hörl, W. H. (2007) Clinical Aspects of Iron Use in the Anemia of Kidney Disease. *Journal of the American Society of Nephrology*, **18(2)**, 382–393.

13. Agarwal, R., Vasavada, N., Sachs, N. G. and Chase, S. (2004) Oxidative stress and renal injury with intravenous iron in patients with chronic kidney disease. *Kidney International*, **65(6)**, 2279–2289.

14. van Swelm, R. P. L., Wetzels, J. F. M. and Swinkels, D. W. (2020) The multifaceted role of iron in renal health and disease. *Nature Reviews Nephrology*, **16(2)**, 77–98.

15. Wojtaszek, E., Glogowski, T. and Malyszko, J. (2020) Iron and Chronic Kidney Disease: Still a Challenge. *Frontiers in Medicine*, **7**, 565135–565145.

16. Altamura, S. and Muckenthaler, M. U. (2009) Iron toxicity in diseases of aging: Alzheimer's disease, Parkinson's disease and atherosclerosis. *Journal of Alzheimer's Disease: JAD*, **16(4)**, 879–895.

17. Duce, J. A. (2010) Iron-export ferroxidase activity of β-amyloid precursor protein is inhibited by zinc in Alzheimer's disease. *Cell*, **142(6)**, 857–867.

18. Guo, S., Chen, F., Yin, X., Wang, L., Guo, X., Yu, Q., Zou Z., and Shu, W. (2022) Developments in the Role of Iron Imbalance in the Pathogenesis of Alzheimer's Disease. *Chinese General Practice Journal*, **25(3)**, 373–379.

19. Weinstein, D. A., Roy, C. N., Fleming, M. D., Loda, M. F., Wolfsdorf, J. I. and Andrews, N. C. (2002) Inappropriate expression of hepcidin is associated with iron refractory anemia: implications for the anemia of chronic disease. *Blood*, **100(10)**, 3776–3781.

20. Yang, J., Li, Q., Feng, Y. and Zeng, Y. (2023) Iron Deficiency and Iron Deficiency Anemia: Potential Risk Factors in Bone Loss. *International Journal of Molecular Sciences*, **24(8)**, 6891.

21. Basak, T. and Kanwar, R. K., (2022) Iron imbalance in cancer: Intersection of deficiency and overload. *Cancer Medicine*, **11(20)**, 3837–3853.

22. Salnikow, K. (2021) Role of iron in cancer. *Seminar in Cancer Biology*, **76**, 189–194.

23. Narayanaswamy, N. and Govindaraju, T. (2012) Aldazine-based colorimetric sensors for Cu^{2+} and Fe^{3+}. *Sensors and Actuators B: Chemical*, **161(1)**, 304–310.

24. Duvigneau, J. C., *et al.* (2008) A novel endotoxin-induced pathway: upregulation of heme oxygenase 1, accumulation of free iron, and free iron-mediated mitochondrial dysfunction. *Laboratory Investigation*, **88(1)**, 70–77.

25. Sucak, G. T., Yegin, Z. A., Ozkurt, Z. N., Aki, S. Z., Karakan, T. and Akyol, G. (2008) The role of liver biopsy in the workup of liver dysfunction late after SCT: is the role of iron overload underestimated? *Bone Marrow Transplant*ation, **42(7)**, 461–467.

26. Lu, M. and Compton, R. G. (2013) Voltammetric Determination of Iron(III) in Water. *Electroanalysis*, **25(5)**, 1123–1129.

27. Paut, A., Prkić, A., Mitar, I., Bošković, P., Jozić, D., Jakić, M. and Vukušić, T. (2021) Potentiometric Response of Solid-State Sensors Based on Ferric Phosphate for Iron(III) Determination. *Sensors*, **21(5)**, 1612.

28. Shahat, A., Elamin, N. Y. and Abd El-Fattah, W. (2021) Spectrophotometric and Fluorometric Methods for the Determination of Fe(III) Ions in Water and Pharmaceutical Samples. *ACS Omega*, **7(1)**, 1288–1298.

29. Mogwasi, R., Mobegi, E. O. M. E. and Nyabaro, O. (2023) Inductively coupled plasma-mass spectrometry versus flame atomic absorption spectrophotometry for the analysis of Fe, Cu, Zn, Mn and Cr in medicinal plants: a comparison study. *Advances in Translational Medicine*, **2(1)**, 1–15.

30. Hamishehkar, H., Ghasemzadeh, B., Naseri, A., Salehi, R. and Rasoulzadeh, F. (2015) Carbon dots preparation as a fluorescent sensing platform for highly efficient detection of Fe(III) ions in biological systems. *Spectrochimica Acta. Part A, Molecular and Biomolecular Spectroscopy*, **150**, 934–939.

31. Li, L., Lyu, X., Liang, S. and Liu, Z. (2023) Application of fluorescence sensing technology in trace detection of explosives. *Dyes and Pigments*, **220**, 111651–111667.

32. Ashley, J. and Manikova, P. (2023) Fluorescent sensors. *Fundamentals of Sensor Technology*, 147–161.

33. Gupta, R. and Xie, H. (2018) Nanoparticles in daily life: applications, toxicity and regulations. *Journal of Environmental Pathology, Toxicology and Oncology*, **37(3)**, 209–230.

34. Anik, M. I., Mahmud, N., Al Masud, A. and Hasan, M. (2022) Gold nanoparticles (GNPs) in biomedical and clinical applications: A review. *Nano Select*, **3(4)**, 792–828.

35. Adil, L. R., Parui, R., Khatun, M. N., Chanu, M. A., Li, L., Wang, S. and Iyer, P. K. (2022) Nanomaterials for sensors: Synthesis and applications. In *Advanced Nanomaterials for Point of Care Diagnosis and Therapy*, 121–168.

36. Singh, M., Goyal, M. and Devlal, K. (2018) Size and shape effects on the band gap of semiconductor compound nanomaterials. *Journal of Taibah University for Science*, **12(4)**, 470–475.

37. Abdullah, B. J. (2022) Size effect of band gap in semiconductor nanocrystals and nanostructures from density functional theory within HSE06. *Materials Science in Semiconductor Processing*, **137**, 106214–106224.

38. Saravanan, R. S. S., Pukazhselvan, D. and Mahadevan, C. K. (2012) Studies on the synthesis of cubic ZnS quantum dots, capping and optical–electrical characteristics. *Journal of Alloys and Compounds*, **517**, 139–148.

39. Dong, B., Cao, L., Su, G., Liu, W., Qu, H. and Zhai, H. (2010) Water-soluble ZnS: Mn/ZnS core/shell nanoparticles prepared by a novel two-step method. *Journal of Alloys and Compounds*, **492(1-2)**, 363–367.

40. Wang, X. F., Xu, J. J. and Chen, H. Y. (2008) A new electrochemiluminescence emission of Mn^{2+}-doped ZnS nanocrystals in aqueous solution. *The Journal of Physical Chemistry C*, **112(45)**, 17581–7585.

41. Lü, C., Gao, J., Fu, Y., Du, Y., Shi, Y. and Su, Z. (2008) A ligand exchange route to highly luminescent surface-functionalized ZnS nanoparticles and their transparent polymer nanocomposites. *Advanced Functional Materials*, **18(19)**, 3070–3079.

42. Javed, R., Zia, M., Naz, S., Aisida, S. O., Ain, N. U. and Ao, Q. (2020) Role of capping agents in the application of nanoparticles in biomedicine and environmental remediation: recent trends and future prospects. *Journal of Nanobiotechnology*, **18**, 1–15.

43. Ayodhya, D. and Veerabhadram, G. (2019) Fabrication of Schiff base coordinated ZnS nanoparticles for enhanced photocatalytic degradation of chlorpyrifos pesticide and detection of heavy metal ions. *Journal of Materiomics*, **5(3)**, 446–454.

44. Nagel, J., Oertel, U., Friedel, P., Komber, H. and Möbius, D. (1997) Langmuir− Blodgett Layers from Schiff Base Copper (II) Complexes. *Langmuir*, **13(17)**, 4693–4698.

45. Ayodhya, D., Venkatesham, M., Kumari, A. S., Mangatayaru, K. G. and Veerabhadram, G. (2013) Synthesis, characterization of ZnS nanoparticles by coprecipitation method using various capping agents—photocatalytic activity and kinetic study. *Journal of Applied Chemistry*, **6(1)**, 101–109.

46. Adhikari, J., Bhattarai, A. and Chaudhary, N. K. (2022) Synthesis, characterization, physicochemical studies, and antibacterial evaluation of surfactant-based Schiff base transition metal complexes. *Chemical Papers*, **76(4)**, 2549–2566.

47. Won, S. and Kim, J. (2022) The detection of Fe (III) and ascorbic acid by fluorescence quenching and recovery of carbon dots prepared from coffee waste. *Korean Journal of Chemical Engineering*, **39(10)**, 2826–2833.

48. Zhang, X., Li, C., Zhao, S., Pang, H., Han, Y., Luo, X., Tang, W. and Li, Z. (2020) S doped silicon quantum dots with high quantum yield as a fluorescent sensor for determination of Fe^{3+} in water. *Optical Materials*, **110**, 110461.

49. Ayodhya, D. and Veerabhadram, G. (2018) Synthesis and characterization of N, O-donor Schiff base capped ZnS NPs as a sensor for fluorescence selective detection of Fe^{3+}, Cr^{2+} and Cd^{2+} ions. *Modern Electronic Materials*, **4(4)**, 151–162.

50. Sharma, P., Bhogal, S., Mohiuddin, I., Yusuf, M. and Malik, A. K. (2022) Fluorescence "turn-off" sensing of iron (III) Ions utilizing pyrazoline based sensor: Experimental and computational study. *Journal of Fluorescence*, **32(6)**, 2319–2331.

51. Lei, S., Chang, N., Zhang, J. and Wang, H. (2021) Dopamine functionalized S, N co-doped carbon dots as a fluorescent sensor for the selective detection of Fe^{3+} and Fe^{2+} in water. *Analytical Sciences*, **37(6)**, 851–857.

52. Jose, A. R., Sivasankaran, U., Menon, S. and Kumar, K. G. (2016) A silicon nanoparticle based turn off fluorescent sensor for sudan I. *Analytical Methods*, **8(28)**, 5701–5706.

53. Wei, X., Zhou, Z., Hao, T., Li, H., Dai, J., Gao, L., Zheng, X., Wang, J. and Yan, Y. (2015) Simple synthesis of thioglycolic acid-coated CdTe quantum dots as probes for Norfloxacin lactate detection. *Journal of Luminescence*, **161**, 47–53.

54. Genovese, D., Cingolani, M., Rampazzo, E., Prodi, L. and Zaccheroni, N. (2021) Static quenching upon adduct formation: a treatment without shortcuts and approximations. *Chemical Society Reviews*, **50(15)**, 8414–8427.

55. Lakowicz, J. R. (1983) Quenching of fluorescence. *Principles of Fluorescence Spectroscopy*, *Springer New York, New York*, 257–301.

56. Zu, F., Yan, F., Bai, Z., Xu, J., Wang, Y., Huang, Y. and Zhou, X. (2017) The quenching of the fluorescence of carbon dots: a review on mechanisms and applications. *Microchimica Acta*, **184**, 1899–1914.

57. Ahmad, A., Kurkina, T., Kern, K. and Balasubramanian, K. (2009) Applications of the static quenching of rhodamine B by carbon nanotubes. *ChemPhysChem*, **10(13)**, 2251–2255.

58. Mohan, B., Shanmughan, A., Krishna, A. V., Noushija, M. K., Umadevi, D. and Shanmugaraju, S. (2024) Porous organic polymers-based fluorescent chemosensors for Fe (III) ions-a functional mimic of siderophores. *Frontiers in Chemistry*, **12**, 1361796.

59. Lv, R., Chen, Z., Fu, X., Yang, B., Li, H., Su, J., Gu, W. and Liu, X. (2018) A highly selective and fast-response fluorescent probe based on Cd-MOF for the visual detection of Al^{3+} ion and quantitative detection of Fe^{3+} ion. *Journal of Solid State Chemistry*, **259**, 67–72.

60. Yan, F., Zou, Y., Wang, M., Mu, X., Yang, N. and Chen, L. (2014) Highly photoluminescent carbon dots-based fluorescent chemosensors for sensitive and selective detection of mercury ions and application of imaging in living cells. *Sens. Actuators B Chem.*, **192**, 488–495.